Wave-Driven Wind Jets in the Marine Atmospheric Boundary Layer

KIRSTY E. HANLEY AND STEPHEN E. BELCHER

Department of Meteorology, University of Reading, Reading, United Kingdom

(Manuscript received 13 July 2007, in final form 10 December 2007)

ABSTRACT

The interaction between ocean surface waves and the overlying wind leads to a transfer of momentum across the air–sea interface. Atmospheric and oceanic models typically allow for momentum transfer to be directed only downward, from the atmosphere to the ocean. Recent observations have suggested that momentum can also be transferred upward when long wavelength waves, characteristic of remotely generated swell, propagate faster than the wind speed. The effect of upward momentum transfer on the marine atmospheric boundary layer is investigated here using idealized models that solve the momentum budget above the ocean surface. A variant of the classical Ekman model that accounts for the wave-induced stress demonstrates that, although the momentum flux due to the waves penetrates only a small fraction of the depth of the boundary layer, the wind profile is profoundly changed through its whole depth. When the upward momentum transfer from surface waves sufficiently exceeds the downward turbulent momentum flux, then the near-surface wind accelerates, resulting in a low-level wave-driven wind jet. This increases the Coriolis force in the boundary layer, and so the wind turns in the opposite direction to the classical Ekman layer. Calculations of the wave-induced stress due to a wave spectrum representative of fast-moving swell demonstrate upward momentum transfer that is dominated by contributions from waves in the vicinity of the peak in the swell spectrum. This is in contrast to wind-driven waves whose wave-induced stress is dominated by very short wavelength waves. Hence the role of swell can be characterized by the inverse wave age based on the wave phase speed corresponding to the peak in the spectrum. For a spectrum of waves, the total momentum flux is found to reverse sign and become upward, from waves to wind, when the inverse wave age drops below the range 0.15–0.2, which agrees reasonably well with previously published oceanic observations.

1. Introduction

Understanding the dynamical processes that occur in the lower atmosphere and upper ocean is important for a full understanding of air–sea interaction. Correct parameterization of the air–sea momentum fluxes in the atmospheric boundary layer is important for atmospheric, oceanic, and wave models. Currently, large-scale models only allow the momentum flux, τ_{tot}, to be positive, from atmosphere to ocean. Recent observations have reported unusual behavior during conditions of light winds (less than 2 m s^{-1}) and fast-traveling swells, namely upward momentum transfer from the ocean to the atmosphere (Grachev and Fairall 2001) and the occurrence of low-level wind jets (Smedman et al. 1999). Such features are thought to be characteristic of a wave-driven wind regime. This regime was first reported by Harris (1966), who found that in laboratory wave tank experiments, a progressive water wave led to airflow directly above the waves with a mean component in the direction of wave propagation: *a wave-driven wind.* Such wave-driven winds are the subject of this paper.

In nature, ocean waves exist over a broad range of frequencies with contributions from both wind waves and swell. Wind waves are locally generated, short wavelength waves that travel slower than the wind and therefore act as sinks of momentum. In contrast, swell waves are usually remotely generated by distant storms and propagate for thousands of kilometers. There is evidence from calculations and observations to show that swell waves can be associated with upward momentum transfer from ocean to atmosphere. During the Surface Wave Dynamics Experiment, Donelan et al. (1997) measured the air–sea momentum flux via eddy

Corresponding author address: Kirsty E. Hanley, Department of Meteorology, University of Reading, Earley Gate, P.O. Box 243, Reading RG6 6BB, United Kingdom.
E-mail: k.e.hanley@rdg.ac.uk

DOI: 10.1175/2007JAS2562.1

correlation. The measurements were obtained from a mast on the deck of a ship in deep water off the coast of Virginia. They found that swell aligned with the wind can deliver momentum to the atmosphere. Measurements of the stress by Drennan et al. (1999) in Lake Ontario show that for swell aligned with the wind, the stress may be near-zero and sometimes negative. Smedman et al. (1994) describe a case in the Baltic Sea of a near-neutrally stratified marine surface layer with no surface shearing stress, that is $\boldsymbol{\tau}_{\text{tot}} \approx 0$. During conditions of low winds and fast waves they found that the momentum flux is negligible and that the mechanical production of turbulence is close to zero. Observations by Smedman et al. (1999, 2003) in the Baltic Sea have shown that for swell-dominated conditions a logarithmic wind profile is no longer observed. They found that during the swell phase there was a wind speed maximum near or below the lowest wind speed measurement of 10 m. From results obtained during several sea expeditions, Grachev and Fairall (2001) found that in the equatorial west Pacific Ocean, upward momentum transfer occurs about 10% of the time. During swell conditions they found that the momentum flux reverses sign at a wind speed of 1.5–2 m s^{-1}. Their results also supported the findings of Donelan et al. (1997) and Drennan et al. (1999) that upward momentum transfer is generally characterized by swell aligned with the wind direction. In summary, in conditions of swell aligned with a weak wind, observations suggest a momentum flux from waves to wind and a low-level wind jet. The Coupled Boundary Layers Air-Sea Transfer (CBLAST) field campaign (Edson et al. 2007) reports that in light wind conditions (less than 4 m s^{-1}), the winds and waves are usually in a state of disequilibrium where the peak phase speed, c_p, exceeds the wind speed, implying that remotely generated swell is present.

In the presence of surface waves the total wind velocity can be separated into three parts: the mean, turbulent, and wave-induced components of the flow (Phillips 1966). The wave-induced component arises because of airflow over the undulating surface. If the equations of motion are then averaged over a wavelength, the total surface stress over the sea, $\boldsymbol{\tau}_{\text{tot}}$, can be written as a linear superposition of three components:

$$\boldsymbol{\tau}_{\text{tot}} = \boldsymbol{\tau}_t + \boldsymbol{\tau}_w + \boldsymbol{\tau}_{\text{visc}}, \tag{1}$$

where $\boldsymbol{\tau}_t$ is the turbulent shear stress, $\boldsymbol{\tau}_w$ is the wave-induced stress (which accounts for the transfer of momentum to the wave), and $\boldsymbol{\tau}_{\text{visc}}$ is the viscous stress, assumed to be negligible here as it is only important in the millimeter above the surface. Well above the surface $\boldsymbol{\tau}_w = 0$ and the total stress equals the turbulent stress. The layer where the wave-induced stress is an appreciable portion of the total stress is called the wave boundary layer (Smedman et al. 2003). In this layer $\boldsymbol{\tau}_t$ is reduced and the observed wind profiles deviate from a logarithmic form. It is generally thought that in pure wind sea conditions the wave boundary layer is typically $O(1 \text{ m})$ (Janssen 1989) but observations by Smedman et al. (1994) and Grachev et al. (2003) have shown that during swell-dominated conditions it may extend much higher.

The wave-induced momentum flux shows a strong dependence on wave age c_p/u_*, or c_p/U_{10} (Belcher and Hunt 1998), where c_p is the wave phase speed at the spectral peak, u_* is the friction velocity, and U_{10} is the 10 m wind speed. According to Pierson and Moskowitz (1964), the sea state can be classified as a young, developing sea if $c_p/U_{10} < 1.2$ or a mature sea when $c_p/U_{10} > 1.2$. Young seas with waves that travel at speeds much less than the wind speed extract momentum from the wind so that $|\boldsymbol{\tau}_w| > 0$. In these cases the flow is analogous to flow over a solid, rough surface and during neutral conditions the resulting wind profile above the wave boundary layer is logarithmic, as observed by Drennan et al. (2003). As wave age increases, $|\boldsymbol{\tau}_w|$ decreases until it reaches zero and reverses sign. This sign reversal occurs when the wave phase speed, c, exceeds the wind speed ($c/U_{10} > 1$); here we refer to these waves as *fast waves.* Analysis by Cohen and Belcher (1999) predict fast waves for $c/u_* > 20$. Based on direct numerical simulation (DNS), Sullivan et al. (2000) found that for a single sinusoidal wave the sign reversal corresponds to a wave age $c/u_* > 14$. Further increases in wave age lead to $\boldsymbol{\tau}_w$ becoming increasingly negative until eventually $|\boldsymbol{\tau}_{\text{tot}}| = |\boldsymbol{\tau}_t| + |\boldsymbol{\tau}_w|$ becomes negative and momentum is transferred from the ocean to the atmosphere. Kudryavtsev and Makin (2004) have developed a model for the wave boundary layer based on these concepts, which demonstrates that in the case of swell aligned with the mean wind direction, a jetlike wind profile is obtained with a maximum at the height of the wave boundary layer.

This paper aims to distinguish how ocean surface waves affect the dynamics of the whole boundary layer using simple models of the momentum budget above the ocean surface. These models will be used to study the effects of negative (i.e., wave to atmosphere) wave-induced stress on the wind profile and to determine whether there are conditions for which the net momentum flux is predominantly negative. This will help determine the importance of wave-driven winds for global climate models.

LES experiments by Sullivan et al. (2008) predict momentum transfer from the ocean to the atmosphere for swell following the wind. They have shown that the generation of a low-level jet results in a near collapse of turbulence above, so that the effects of swell are not just confined to the wave boundary layer but have an impact on the whole atmospheric boundary layer. These simulations have done much to motivate the present work. So the first question we address here is (i) what is the structure of the boundary layer in the presence of a wave-driven jet? We address this question in section 3, where a wave-induced stress is added to the standard Ekman model for the atmospheric boundary layer. The turbulent stress is parameterized using a constant eddy viscosity model. The model illustrates qualitatively that the surface waves change the wind profile over the entire depth of the boundary layer and that when the momentum flux is negative a jet is observed in the u-wind profile. The model is used to study the mechanisms that couple the dynamics of the wave boundary layer to the Ekman layer to control the jet.

A second question is (ii) can we diagnose when a jet will be present in the wind profile? This question is addressed in two ways. In section 3 the simple model is used to derive a condition for when a jet is present in the wind profile. This condition is generalized in section 4 using a more sophisticated model for the wave boundary layer that uses a mixing length model to parameterize the eddy viscosity. We first calculate the wave-induced stress for a single sinusoidal wave, and then we calculate the wave-induced stress for a spectrum of waves to determine whether or not negative wave-induced stress is obtained in oceanic conditions. In section 5 the results of this more sophisticated model are compared with previous observations of the low-wind fast-swell regime.

2. Formulation of the model problem

Consider a neutrally stratified boundary layer with a wind blowing over the sea surface. The aim here is to calculate the time-mean wind profile. Hence, the wind is averaged over many wave periods, so that the average vertical velocity is zero and the waves change the momentum balance of the boundary layer through a wave-induced stress, $\boldsymbol{\tau}_w$ (Phillips 1966). The momentum equation then becomes

$$\begin{aligned} f(v - v_g) + \frac{\partial \tau_{tx}}{\partial z} + \frac{\partial \tau_{wx}}{\partial z} &= 0 \\ -f(u - u_g) + \frac{\partial \tau_{ty}}{\partial z} + \frac{\partial \tau_{wy}}{\partial z} &= 0. \end{aligned} \tag{2}$$

Here u and v are the wind speeds and u_g and v_g are the geostrophic values. The turbulent stress has components τ_{tx} in the x direction and τ_{ty} in the y direction, and the Coriolis parameter, $f = 10^{-4}\ \mathrm{s}^{-1}$, is constant in all simulations.

For simplicity, the following assumptions are made: the geostrophic wind is constant with height; the geostrophic wind, u_g, is taken to be in the x direction; and the wave-induced stress is confined to the x direction so that $\boldsymbol{\tau}_w = (\tau_w, 0)$. The boundary conditions applied to (2) are zero velocity at the wave surface and the wind speed tends to the geostrophic values at large heights:

$$u = 0, v = 0 \text{ on } z = 0; u \rightarrow u_g, v \rightarrow 0 \text{ as } z \rightarrow \infty. \tag{3}$$

The effects of the waves on the boundary layer are represented by methods developed from linear theory [see the review of Belcher and Hunt (1998)]. In the basic state, the water surface is at rest below a fully developed boundary layer with mean velocity u and stress τ_{tot}. This state is then perturbed by introduction of a surface wave and perturbations to the mean flow Δu, $\Delta\tau_{\mathrm{tot}}$, and τ_w are calculated. The sea surface is then treated as a Fourier superposition of waves so that the linear theory calculated for airflow over one wave is superposed over many waves.

Belcher and Hunt (1993) show that the wave-induced stress due to a single sinusoidal wave falls off approximately exponentially with height, so we write

$$\tau_w = \tau_w(0) \exp^{-z/h_i}, \tag{4}$$

where $\tau_w(0)$ is the surface value of the wave-induced stress and h_i is the height of the wave boundary layer. The model is completed with parameterizations for the turbulent stress and the surface value of the wave-induced stress.

3. Constant viscosity model

To understand how the wave-induced stress interacts with the Ekman layer, consider first a simple model problem. The surface value of the wave-induced stress, $\tau_w(0)$, is taken to be a constant specified value, and the turbulent stress, $\boldsymbol{\tau}_t$, is parameterized using a simple first-order closure,

$$\boldsymbol{\tau}_t = K_m \frac{\partial \mathbf{u}}{\partial z}, \tag{5}$$

where K_m is the eddy viscosity, assumed in this section to be constant.

The solution is obtained by writing the momentum equations in complex notation, where $\mathcal{U} = u + iv$:

$$\frac{\partial^2 \mathcal{U}}{\partial z^2} = \frac{if}{K_m}(\mathcal{U} - u_g) - \frac{\tau_w}{K_m h_i}, \tag{6}$$

where τ_w is defined in (4). The equation can be solved analytically, applying the boundary conditions in (3). Following the analysis of Polton et al. (2005), who analyzed the role of waves on the ocean mixed layer, the solution can be decomposed into three parts to show how the waves change the wind profile over the whole depth of the atmospheric boundary layer:

$$\mathcal{U} = \mathcal{U}_e + \mathcal{U}_{\text{ew}} + \mathcal{U}_w, \tag{7}$$

where

$$\mathcal{U}_e = u_g\left\{1 - \exp\left[-(1+i)\frac{z}{h_e}\right]\right\}, \tag{8}$$

$$\mathcal{U}_{\text{ew}} = -\frac{\tau_w(0)h_i}{K_m(1 - i2h_i^2/h_e^2)}\exp\left[-(1+i)\frac{z}{h_e}\right], \quad \text{and} \tag{9}$$

$$\mathcal{U}_w = \frac{\tau_w(0)h_i}{K_m(1 - i2h_i^2/h_e^2)}\exp\left(-\frac{z}{h_i}\right). \tag{10}$$

The Ekman depth scale $h_e = (2K_m/f)^{1/2}$ represents the height over which the turbulent stress balances the Coriolis force and the pressure gradient force. Here $\mathcal{U}_e$ is the Ekman solution; this would be the entire solution if the waves were not present. The effect of the waves is to introduce two new terms into the solution. The wave-induced component, $\mathcal{U}_w$, is forced directly by the wave-induced stress and decays over the depth of the wave boundary layer, h_i. Mathematically it is the particular integral to the forcing by the wave-induced stress. There is also an Ekman-wave component, $\mathcal{U}_{\text{ew}}$, that decays over the depth of the whole boundary layer and therefore modifies the wind profile throughout the entire depth of the boundary layer. The Ekman-wave component, $\mathcal{U}_{\text{ew}}$, arises as a response to the wave-induced component, $\mathcal{U}_w$: the wave-induced component produces a surface wind, and the Ekman-wave component is required to remove the surface wind to ensure that the total solution satisfies the surface boundary condition. In this sense the waves change the boundary condition on the Ekman layer and thus change the wind profile through the whole layer.

The decomposition of the solution for the wind profile in the case of a negative (i.e., wave to wind) wave-induced stress for illustrative parameter values is shown in Fig. 1. Parameter values are explored in more detail in section 4. The full solution is shown by the solid line, the dashed line represents the Ekman component, the dotted–dashed line represents the Ekman-wave component, and the dotted line represents the wave component. The wave component of the solution is nonzero only in the lower fraction of the boundary layer (the so-called wave boundary layer), whereas the Ekman-wave component of the solution penetrates the entire depth of the boundary layer. The full solution is observed to turn in the opposite direction to the Ekman solution ($v < 0$, $v_e > 0$). In the full solution, a low-level supergeostrophic jet is seen in the u-wind profile. Above the jet the wind speed reduces smoothly to the geostrophic wind. The jet occurs at the height at which the wave solution becomes zero (i.e., a height of the order $2h_i$). These features are in qualitative agreement with the large-eddy simulation (LES) results of Sullivan et al. (2008).

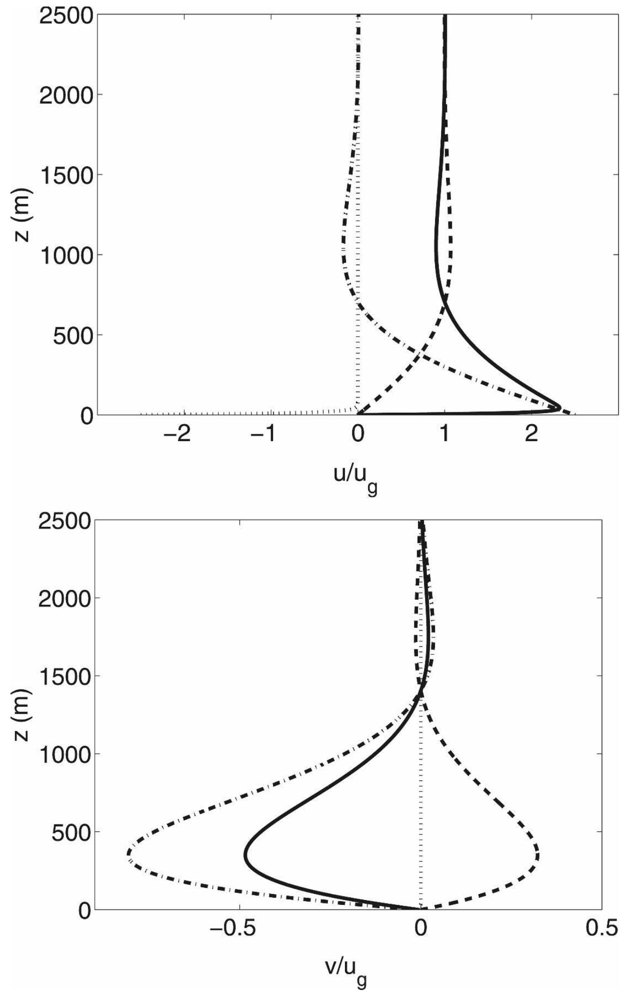

FIG. 1. The velocity components for a solution to the constant eddy viscosity model: (top) u/u_g and (bottom) v/u_g. The parameters are K_m = 10 m^2 s^{-1}, $f = 10^{-4}$ s^{-1}, u_g = 2 m s^{-1}, h_i = 10 m, and $\tau_w(0)$ = −5 N m^{-2}. The solid line is the full solution, the dashed line is the Ekman component, the dotted–dashed line is the Ekman-wave component, and the dotted line is the wave component.

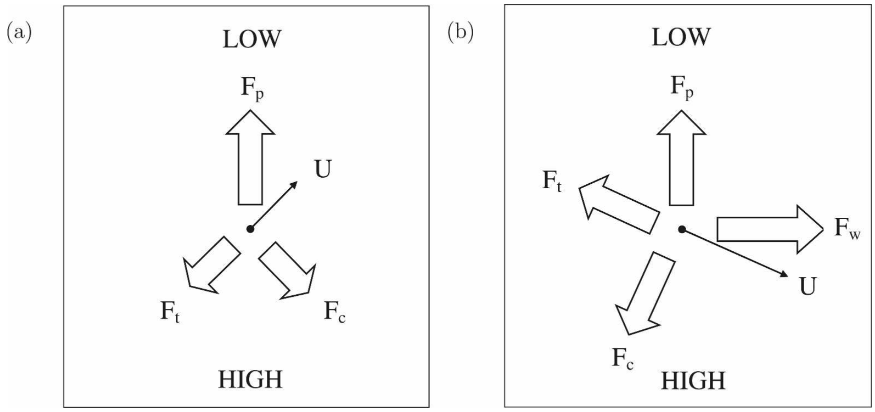

FIG. 2. Schematic to show the (a) force balance in the Ekman case and (b) main mechanism that produces wave-driven winds. Here F_p represents the pressure gradient force, F_c represents the Coriolis force, F_t represents friction due to turbulent stresses, and F_w represents friction due to the wave-induced stress.

The wind profiles are a result of a balance between three forces: the pressure gradient force, $\mathbf{F}_p$; the Coriolis force, $\mathbf{F}_c$; and the force exerted by the stress gradient. Far above the surface there is a geostrophic balance between the pressure gradient and Coriolis forces, resulting in the geostrophic wind. In the Ekman case (Fig. 2a), the stress, $\boldsymbol{\tau}_t$, because of turbulence, acts as a drag on the surface that reduces the surface wind. The Coriolis force has magnitude fU; therefore reducing the wind speed reduces the magnitude of $\mathbf{F}_c$. The pressure gradient is unchanged and therefore causes an acceleration toward the low. Figure 2a shows that to balance the turbulent stress and the pressure gradient force, the Coriolis force must change direction. As a result, a new steady state is achieved where the near-surface wind turns toward the low pressure.

Over the ocean, the total stress is partitioned between a turbulent part, $\boldsymbol{\tau}_t$, and a wave-induced part, $\boldsymbol{\tau}_w$. When the waves travel faster than the wind, the wave-induced stress is negative. The gradient of the wave-induced stress is, however, positive and thus accelerates the wind over the depth of the wave boundary layer, h_i. If the magnitude of $\boldsymbol{\tau}_w$ is then greater than the magnitude of $\boldsymbol{\tau}_t$, there is a net upward momentum flux that accelerates the surface wind. This acceleration leads to a wave-driven jet with a maximum wind speed at the top of the wave boundary layer, at a height of approximately h_i. Figure 2b shows that in this case the Coriolis force increases and must turn in the opposite direction to balance the other forces. The response of the wind is to turn toward the high pressure (toward the right). This is illustrated in Fig. 3, which shows a hodograph of the solutions. The solid line shows the solution for waves traveling faster than the wind and the dashed line shows the solution for the Ekman case. The surface wind turns to the left in the Ekman solution and to the right when fast-traveling waves are present.

The analytical solution can be used to diagnose when a jet is observed. Normally in the atmospheric boundary layer $h_i \ll h_e$ so that $1 - 2ih_i^2/h_e^2 \approx 1$. Above the wave boundary layer $z > h_i$, so in this case the solution is approximately the sum of the Ekman component and the Ekman-wave component:

$$\mathcal{U} \approx u_g\left\{1 - \left[1 + \frac{\tau_w(0)h_i}{u_g K_m}\right]\exp\left[-(1+i)\frac{z}{h_e}\right]\right\}. \tag{11}$$

The wave-induced stress forces a maximum wind speed of

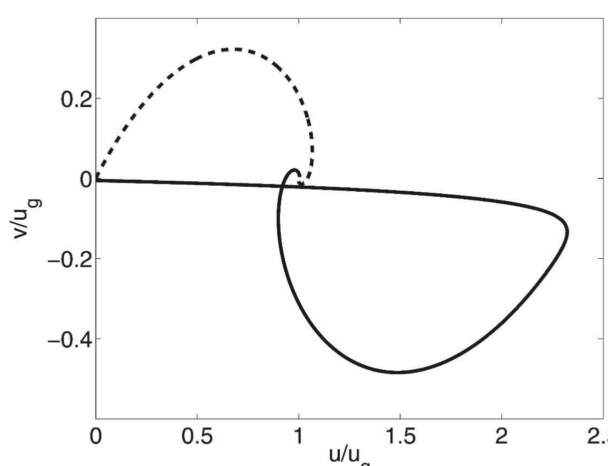

FIG. 3. Hodograph for a solution to the constant eddy viscosity model. The parameters are $K_m = 10\ \mathrm{m^2\ s^{-1}}$, $f = 10^{-4}\ \mathrm{s^{-1}}$, and $u_g = 2\ \mathrm{m\ s^{-1}}$. The solid line is the solution for waves traveling faster than the wind, $\tau_w(0) = -5\ \mathrm{N\ m^{-2}}$, and the dashed line is the Ekman solution, $\tau_w(0) = 0\ \mathrm{N\ m^{-2}}$.

$$u_w = \frac{-\tau_w(0)h_i}{K_m}. \tag{12}$$

Hence, for a negative wave-induced stress, u_w is positive. Furthermore, a wave-induced jet is forced when $u_w > u_g$.

4. Mixing length model

The solutions obtained with the simple model of section 3 are expected to provide the correct qualitative effects of the wave-induced stress. To substantiate this claim a more sophisticated model is now developed. Again this is a simple model, that just contains the Ekman dynamics with the addition of the wave-induced stress, but now the turbulent stress is more realistically modeled using a mixing length model. Furthermore, the wave-induced stress is calculated rather than specified. This ensures that it is better represented than in section 3 where it is simply an input parameter to the model.

The mixing length model for the eddy viscosity, K_m, depends on height, wind shear, and stability. As only neutral boundary layers are considered here, the stability dependence of K_m can be ignored. The justification for using a mixing length model rests partly on simplicity and partly on the analysis of Cohen and Belcher (1999), who justify its use in a linear theory when the effects of the waves are small. Within the inner region there is approximate balance between the production and dissipation of turbulent kinetic energy, and so a mixing length model is justified. Now, K_m is calculated as

$$K_m = l_m^2 \left| \frac{\partial \mathbf{u}}{\partial z} \right|, \tag{13}$$

where l_m is the mixing length. Near the surface l_m depends only on the distance from the surface, $l_m = \kappa z$, where κ is von Kármán's constant. Higher up $l_m = l_0$, where l_0 is a constant, taken here to be 300 m. Tests with the model have shown that the results are not sensitive to the value of l_0 chosen. These can be combined to give the Blackadar mixing length

$$l_m^{-1} = [\kappa(z + z_0)]^{-1} + l_0^{-1}, \tag{14}$$

where z_0 is the roughness length of the surface. The roughness length is calculated using Charnock's formula for rough flow patched onto the smooth flow formula (Donelan 1990)

$$z_0 = \left(\frac{0.1\nu}{u_*} + \frac{\alpha_c u_*^2}{g} \right), \tag{15}$$

where ν is the kinematic viscosity of air, 1.4×10^{-5} m^2 s^{-1}, and α_c is the Charnock coefficient, taken here to be 0.012.

The wave-induced stress acts on the boundary layer flow within the wave boundary layer of depth h_i. Cohen and Belcher (1999) show that for both slow and fast waves the depth of the wave boundary layer is well approximated by

$$kh_i \approx 0.1. \tag{16}$$

According to Makin et al. (1995), the surface value of the wave-induced stress is given by integration of the wave-induced stress going into each wave component:

$$\tau_w(0) = \int_0^\infty \rho_w \omega \beta \Phi(\omega)\, d\omega, \tag{17}$$

where ω is the wave angular frequency, $\Phi(\omega)$ is the frequency spectrum, and β is the dimensionless wave growth rate parameter.

The wave growth rate parameter describes the rate of growth or decay of a wave spectral component of wavenumber k; it is written by Belcher and Hunt (1993) as

$$\beta = \frac{\dot{E}}{E} = c_\beta \omega \frac{\rho_a}{\rho_w} \left(\frac{u_*}{c} \right)^2, \tag{18}$$

where E is wave energy, c_β is the wave growth rate coefficient, c is the wave phase speed, and u_* is the friction velocity at the surface. The motion of the water leads to an orbital velocity at the surface that is of the order akc, where a is the wave amplitude. These motions distort the airflow and thereby contribute to the growth of the wave. Belcher and Hunt (1993) and Cohen and Belcher (1999) have shown that the effect that varying the orbital velocities has on the wave-averaged flow calculated here is to change the value of the wave growth rate coefficient, c_β, but not the functional form given in (18). Belcher and Hunt (1998) have shown that this term is a function of c/u_*. Plant (1982) compiled wave tank experimental data and open ocean observations from various sources and concluded that in the range of wind speeds for which $c/u_* < 20$, the growth rate is $c_\beta = 32 \pm 16$. In their Fig. 8, Belcher and Hunt (1998) compare the measured growth rate coefficients collected by Plant (1982) with the linear theory for slow waves developed by Belcher and Hunt (1993) and the second-order closure model of Mastenbroek (1996). Although the growth rate coefficient has the same variation with c/u_*, the coefficient obtained from theory is a factor of 2 to 3 smaller than the coefficient obtained from measurements.

Computations by Mastenbroek (1996) and the theory of Cohen and Belcher (1999) have shown that for fast waves (i.e., $c/u_* > 20$) the wave growth rate coefficient is negative. Belcher and Hunt (1993) and Mastenbroek (1996) showed that the calculated values of the growth rate are strongly dependent on the turbulence closure scheme used. In general, a mixing length model yields larger growth rates than a second-order Reynolds stress model. Using a mixing length model, Mastenbroek (1996) calculated the growth rate coefficient for fast waves to be ≈ -15; using a second-order Reynolds stress model a value of ≈ -5 was obtained. The theory of Cohen and Belcher (1999) predicts growth rates of ≈ -10 for fast waves. In agreement with Mastenbroek (1996) and Belcher and Hunt (1993), Cohen and Belcher (1999) have found that the theoretical growth rates underestimate the experimental growth rates for wind-driven waves. Therefore, we pose the following question: is it possible that theory also underestimates the decay rates for fast waves? Hasselmann and Bosenberg (1991) made measurements over a wide range of c/u_* in the ocean. Their measurements were not sufficiently accurate to detect growth or decay of fast waves. We are not aware of any other measurements of the growth rate coefficient for fast waves aligned with the wind to compare with the theory. Pierson and Moskowitz (1964) present laboratory measurements of wave attenuation rates due to an opposing wind; again it is found that theory underestimates the attenuation rates by a factor of 3.

Consequently, here the wave growth rate coefficient has been parameterized in a simple way so that for slow waves (i.e., $c/u_* < 20$) $c_\beta = 32$, and given the uncertainty in the value, we have chosen a relatively large value of $c_\beta = -30$ for fast waves (i.e., $c/u_* > 20$). The final results are sensitive to the value of c_β chosen and smaller values show less tendency to form wave-driven winds. But wave-driven winds have been observed over the ocean; therefore, we have chosen a value of c_β for fast waves that allows wave-driven jets to develop in the model. In doing so, we hope that the present calculations may provide a constraint on the value of c_β for wave-driven winds.

The friction velocity is defined in terms of the magnitude of the turbulent stress at the surface, $\rho_a u_*^2 = \tau_t(0)$. This approach is taken because the profile is logarithmic below the jet. For consistency with section 3, the waves are confined to the x direction. Since the mean wind direction and therefore $\tau_t(0)$ are at an angle, θ, to the mean direction of propagation of the waves, it is only the component of u_* in the direction of the waves that contributes to $\tau_w(0)$, that is, $u_*^2 \cos(\theta)$ (Meirink and Makin 2000). Typically for fast waves $\theta < 5°$, so that $\cos(\theta) \approx 1$.

a. Wave-induced stress for a single sinusoidal wave

To compare the wind profiles obtained when using this more sophisticated model with the results of section 3, the analysis has first been performed for a single sinusoidal wave. Assuming a linear dispersion relation, for a single wave (17) can be written as

$$\tau_w(0) = \frac{1}{2} c_\beta (ak)^2 u_*^2 \cos(\theta). \tag{19}$$

Since $\tau_w(0) \propto u_*^2 = \tau_t(0)$, the wave-induced stress is now computed by the model as part of the solution.

The model has been used to study a neutrally stratified boundary layer over ocean waves. Three cases have been considered: the standard Ekman case where the waves are not present; a case with low wind and fast waves (i.e., $c_\beta = -30$) that produce negative wave-induced stress; and a case with high wind and slow waves (i.e., $c_\beta = 32$) that produce positive wave-induced stress. The height of the wave boundary layer is calculated using (16). The remaining input parameters to the model are the wave amplitude and the wavenumber. In the standard Ekman case there is no wave present so a and k are both specified as 0. The geostrophic wind is set at $u_g = 10$ m s^{-1}. In the case of fast and slow waves a constant wave slope of $ak = 0.2$ is chosen so that the main difference in the calculation of $\tau_w(0)$ in each case is the value of c_β. For the fast waves a wavenumber of $k = 0.05$ rad m^{-1} (corresponding to a wavelength of about 125 m and a phase speed of 14 m s^{-1}) is chosen and an amplitude of $a = 4$ m. The geostrophic wind is set at $u_g = 2$ m s^{-1}. For the slow waves a wavenumber of $k = 1$ rad m^{-1} is chosen (corresponding to a wavelength of about 6 m and a phase speed of about 3 m s^{-1}). The geostrophic wind is set at $u_g = 10$ m s^{-1}.

The results are shown in Fig. 4. Fast waves produce negative wave-induced stress that acts to accelerate the airflow and a near-surface supergeostrophic jet $u/u_g > 1.15$ is observed in the u-wind profile at a height of $z = 5$ m, corresponding to approximately $2h_i$. Above the jet the wind speed reduces with height and tends to the geostrophic wind. The surface wind turns toward the high pressure ($v < 0$) as demonstrated by the constant viscosity model. As before, the impact of the waves is not confined to the surface layer but extends throughout the entire depth of the atmospheric boundary layer. These results are in qualitative agreement with the LES predictions of Sullivan et al. (2008), who obtain a low-level jet $u/u_g > 1.1$ at $z \approx 20$ m for a fast wave leading the wind. The wind profiles show the same qualitative forms as those obtained using the constant viscosity model (e.g., when the total stress is negative there is a

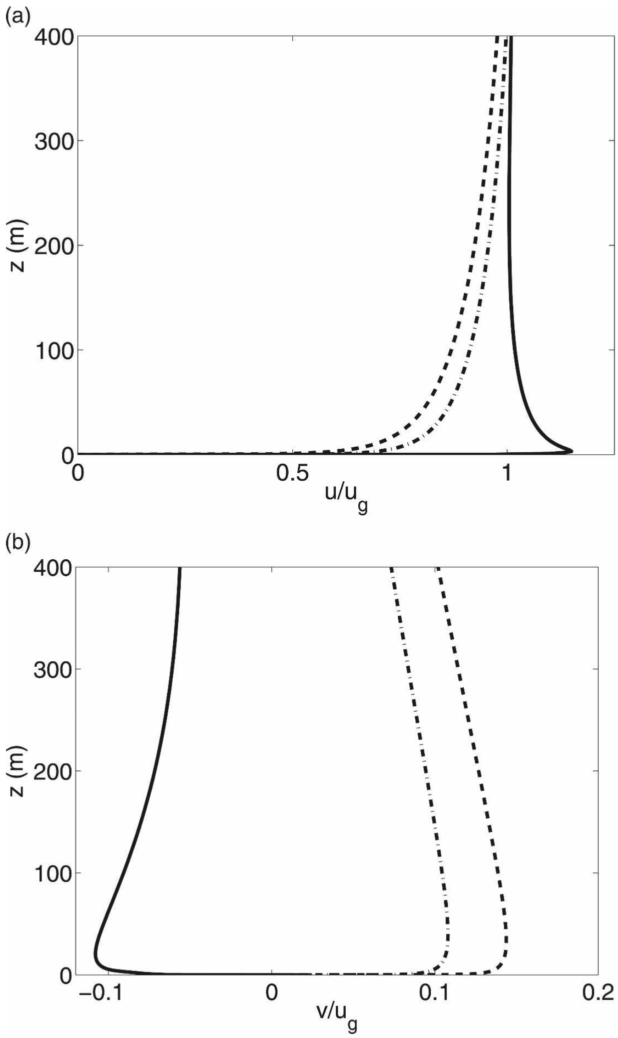

FIG. 4. The solutions to the mixing length model for a single sinusoidal wave: (a) u/u_g and (b) v/u_g vs z. The dotted–dashed line shows the standard Ekman solution with no waves present, the dashed line shows the solution for the slow waves (i.e., $c_\beta = 32$), and the solid line shows the solution for the fast waves (i.e., $c_\beta = -30$).

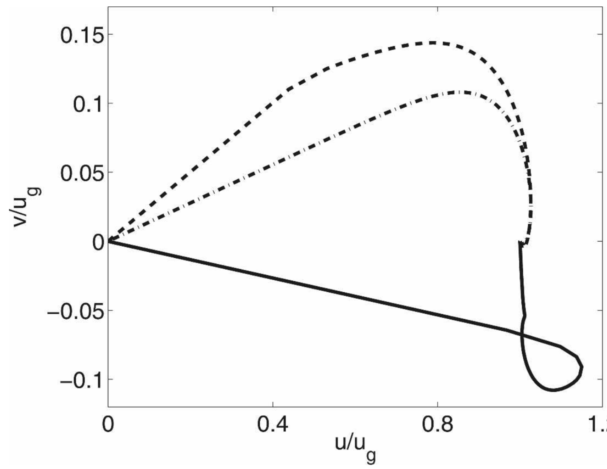

FIG. 5. Hodograph for three solutions to the mixing length model. The dotted–dashed line shows the Ekman solution, the dashed line shows the solution for the slow waves ($c_\beta = 32$), and the solid line shows the solution for the fast waves ($c_\beta = -30$).

low-level supergeostrophic jet and the wind turns in the opposite direction to the standard Ekman spiral). The main features of the wind profile follow through irrespective of the turbulence closure method chosen. The quantitative features, such as the height and strength of the jet, do vary depending on the turbulence closure method. The main differences to the simple model of section 3 are the details of the profile: the jet produced using this model is closer to the surface because the eddy viscosity is reduced near the surface, resulting in greater wind shear.

This model also shows that the slow waves that produce positive wave-induced stress act to decelerate the surface wind (the dashed line in Fig. 4). In this case the surface waves are acting to oppose the surface wind and increase the total surface stress, τ_{tot}, to a greater magnitude than in the case with no waves present. As a result the surface wind in the u direction is reduced more when the air flows over slow waves than when moving over a flat surface. Hence the Coriolis force is also reduced more in this case. As explained in section 3, the smaller the magnitude of the Coriolis force, the more the wind turns from geostrophic; therefore the wind turns further toward the low in the slow-wave case than in the Ekman case. This is illustrated by the hodograph in Fig. 5. The hodograph for the fast-wave case where a wave-driven wind is produced is similar to the hodograph obtained when using the constant viscosity model. The main difference is that with the eddy viscosity model, the wave-driven jet is not exactly aligned with the wave-induced stress.

b. *Wave-induced stress for a spectrum of waves*

In nature, ocean surface waves occur over a broad range of frequencies, described by the frequency spectrum. The portion of spectral components with $c/u_* > 20$ contributes upward momentum flux and the portion with $c/u_* < 20$ produces downward momentum flux. The aim of this section is to build upon the work of Kudryavtsev and Makin (2004) by demonstrating that $\tau_w(0)$ can be negative for a spectrum of waves and then to determine the conditions required for upward momentum transfer.

There is a real question over how to explain theoretically the occurrence of a negative wave-induced stress for a spectrum of waves. The difficulty is best seen by considering the wave-induced stress, or equivalently the drag, associated with flow over wind-driven waves. It is generally accepted that it is the short waves, with frequencies beyond about twice the spectral peak, that provide most of the drag on the airflow (Phillips 1966; Makin et al. 1995; Kukulka and Hara 2005). To see this, consider the wave-induced stress at the surface, which is the sum of the stress going into each Fourier component, namely (17). Using the linear dispersion relation and evaluating β using (18), Eq. (17) yields

$$\tau_w(0) = \int_0^\infty \frac{c_\beta u_*^2}{g^2}\,\omega^4 \Phi(\omega)\,\mathrm{d}\omega. \qquad (20)$$

This integral shows clearly that in wind-driven waves the wave-induced stress comes from the high-frequency, short-wavelength waves because of the ω^4 weighting. Phillips (1985) developed a theory to suggest that beyond about twice the peak frequency, the frequency spectrum $\Phi(\omega) \propto \omega^{-4}$; this is a form that is supported by data. Hara and Belcher (2002) show that the spectrum falls off more rapidly than this at very high frequencies because the very short wavelength waves are sheltered by the longer waves. The result is that the wave-induced stress due to wind-driven waves is dominated by the ω^{-4} region of the spectrum. The physical interpretation is that these waves have steep slopes and are also strongly coupled to the wind. Waves in the vicinity of the spectral peak have lower slopes and are also more weakly coupled to the wind.

So the question is, how can swell, which has low slope and is relatively weakly coupled to the wind, add sufficient upward momentum flux to offset all of the downward momentum flux absorbed by the high-frequency waves in the tail of the spectrum? In their Fig. 4, Smedman et al. (1999) show an observed wave spectrum measured when the local wind speed was 4 m s^{-1}. Also shown on their figure is the corresponding Pierson–Moskowitz theoretical spectrum for this wind speed. The measured spectrum has a much higher peak frequency and higher spectral density than the theoretical spectrum. Therefore the local wind could not have generated the spectrum; it must have been generated remotely. Our interpretation is that (i) storm winds of 10.5 m s^{-1} generate a wind sea with peak wave speed of 8.25 m s^{-1}; (ii) the storm passes and the wind speed drops to 4 m s^{-1}, but the spectrum of waves remains, which we now refer to as swell. The quantitative evidence for this is that the spectrum measured under the low 4 m s^{-1} wind is well represented using the form suggested by Donelan et al. (1985) with the storm conditions of 10.5 m s^{-1}.

Here we propose the following model for the spectrum, motivated by the observations of Smedman et al. (1999): Suppose that a storm produces a spectrum of waves. Once the storm has passed the waves propagate at their group speed and also lose their source of energy. Dispersion separates the fast-moving long wavelengths from the slow-moving short wavelengths. In addition, processes such as wave breaking and wave turbulence interaction continue, damping the waves. Since the short waves have less inertia, their dynamical response time is shorter and they are damped quickly. The resulting spectrum is then typical of swell with long waves but very little energy in the short waves. The swell then propagates into a region of light winds and gives conditions conducive to a wave-driven wind.

We now develop a heuristic, but quantitative, model for the wave-induced stress generated in this situation. The frequency spectrum of the wind waves generated by the storm is calculated using the form suggested by Donelan et al. (1985), namely

$$\Phi_0(\omega) = \alpha_d g^2 \omega^{-5} (\omega/\omega_p) \exp(-\omega/\omega_p) \gamma_d^\Gamma, \qquad (21)$$

where

$$\Gamma = \exp[-(\omega - \omega_p)^2 / 2\sigma_d^2 \omega_p^2], \qquad (22)$$

with $\alpha_d = 0.006\,(u_s/c_p)^{0.55}$, $\sigma_d = 0.08[1 + 4/(u_s/c_p)]^3$, $\gamma_d = 1.7 + 6.0 \log\,(u_s/c_p)$, and ω_p is the frequency at the peak of the spectrum. This spectral form relates the spectral components to the peak frequency, ω_p, and the wind forcing parameter u_s/c_p, where u_s is the component of the 10-m wind speed of the storm in the direction of propagation of the waves at the spectral peak and c_p is the corresponding phase speed.

Once the storm passes, the waves lose their source of energy and stop growing. Indeed, dispersion and processes that damp the waves, such as wave breaking and wave turbulence interaction, continue to act. For example, Teixeira and Belcher (2002) show that waves decay when they propagate over oceanic turbulence at a rate given by the same form as (18), which means that the short waves decay faster than the long waves. Integrating (18) and assuming a linear dispersion relation gives the following relation for the decay of wave energy:

$$E = E_0 \exp\left(\frac{c_\beta u_*^2 \omega^3 t}{\rho_w g^2}\right), \qquad (23)$$

where t is an effective damping time. Since we expect the wave spectral power to decay at the same rate as wave energy, this suggests a model where the swell spectrum is represented by

$$\Phi(\omega) = \Phi_0(\omega) \exp\left[\left(\frac{\omega}{\omega_0}\right)^3\right], \tag{24}$$

where ω_0 is a damping parameter, with $\omega_0^{-3} = c_\beta u_*^2 t/\rho_w g^2$. We know that swell propagates thousands of kilometers (Snodgrass et al. 1966) so we expect ω_0^{-3} to be small, so that only short waves are damped, and the longer wavelengths are largely unaffected. Here a value of $\omega_0^{-3} = -0.01$ has been chosen as a compromise that is sufficient to damp out the short-wavelength waves that contribute positive wave-induced stress without damping the longer waves too much. The results presented below are not appreciably changed if this parameter is varied by a factor of 2 bigger or smaller. The result fits with common experience: a sea composed of smooth, long-wavelength swell.

The swell then propagates into a region where the wind speed is low. Therefore, there will also be a contribution to the wave-induced stress from the waves generated by the local wind. Calculations not presented here suggest that this contribution is negligible when compared to the contribution to τ_w from the swell, and as a result has not been included in the current model.

The wave-induced stress is then computed using (20), with the spectrum specified by (24). The model requires the following parameters to be specified: the two wind speeds needed are the wind speed that represents the storm, denoted u_s, and the wind speed in the region of the swell, denoted u_g. The model also requires the phase speed of waves at the peak in the spectrum, c_p.

Does this model produce negative wave-induced stress in realistic conditions? Define a ratio $\alpha = \tau_w(0)/u_*^2$ for a wave-driven jet to be present in the wind profile it is necessary that the wave-induced stress is negative and has magnitude greater than the turbulent stress to ensure that the upward momentum flux from the waves exceeds the downward momentum flux by turbulence. Hence, a necessary condition for a jet is that $\alpha < -1$. Figure 6 shows α computed for different wind speeds. In these calculations, u_s and u_g vary but the peak wave speed, c_p, is kept constant. Typical ocean swells have periods in the range 10–25 s (Grachev and Fairall 2001), corresponding to phase speeds in the range 15–40 m s^{-1}. Therefore the peak wave speed is set at $c_p = 15$ m s^{-1}, corresponding to a wavelength of about 150 m. Since the wind can generate waves with a limiting peak phase speed $c_p = 1.2U_{10}$ (Alves et al. 2003), this requires a storm wind speed $u_s > 12.5$ m s^{-1}, which is typical of a synoptic storm. Figure 6 shows that the condition $\alpha < -1$ is met when the storm wind speed, u_s, is high, so that the dominant waves have plenty of energy, and the value of the local wind, u_g, is low. In these conditions the present model predicts negative wave-induced stress, and hence the possibility of a wave-driven wind.

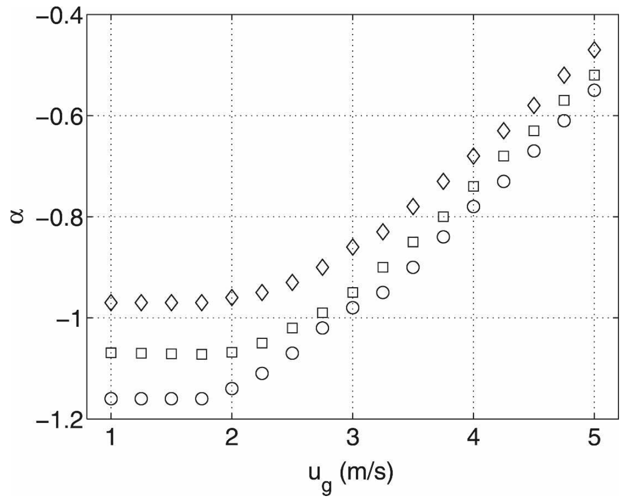

FIG. 6. Variation of α with wind speed, u_g, for different values of the initial wind speed of the storm, u_s. The wave speed is kept constant; in this example $c_p = 15$ m s^{-1}. The circles, squares, and diamonds show $u_s = 20$, 17.5, and 15 m s^{-1}, respectively.

The wave-induced stress, $\tau_w(0)$, normalized on the turbulent stress at the surface, u_*^2, varies with the parameters of the system in the following way: the integral in (20) that determines $\tau_w(0)$ receives a positive contribution ($c_\beta = 32$) from slow waves with $c/u_* < 20$, and a negative contribution ($c_\beta = -30$) from fast waves with $c/u_* > 20$. Hence, the dimensionless ratio $\alpha = \tau_w(0)/u_*^2$ depends on c/u_*. In addition, the shape of the wave spectrum (when normalized on $g^2\omega_p^{-5}$) varies weakly with the wind forcing parameter, u_s/c_p, and the damping parameter, ω_p/ω_0. Overall, α varies strongly with c/u_* and only weakly with u_s/c_p and ω_p/ω_0. Consequently, we expect the condition $\alpha < -1$ to be largely controlled by c/u_*. This idea is tested in section 5.

Figure 7 shows the spectrum of contributions to the wave-induced stress normalized on total stress, $\alpha = \tau_w(0)/u_*^2$. Figure 7a shows α for wind-driven waves, when there is a large contribution to the wave-induced stress from the peak in the spectrum, and also from the tail in the spectrum (as described above; see also Makin et al. 1995). Figure 7b shows α for a wave-driven wind case. There is a large contribution from the peak in the spectrum but the contributions from the tail are smaller and also change sign for very short waves when $c/u_* < 20$, leading to some cancellation. Consequently the dominant contribution is from the peak in the spectrum. Hence, for wave-driven winds the depth of the wave boundary layer and the height of the wind jet are determined by the waves at the peak of the spectrum according approximately to

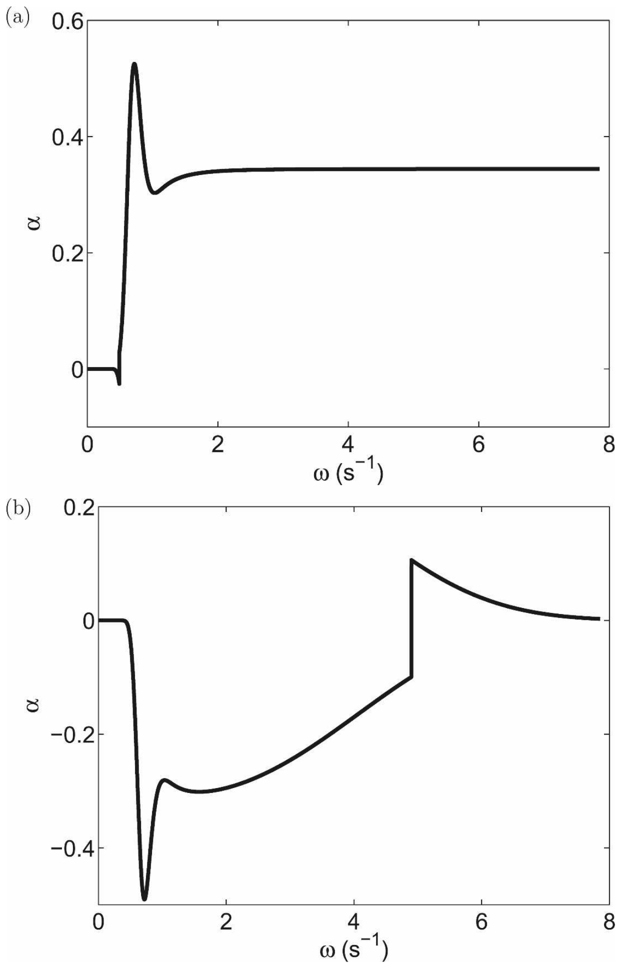

FIG. 7. The spectrum of contributions to the wave-induced stress normalized on total stress α for (a) wind-driven waves and (b) wave-driven winds.

$$h_i = 0.1/k_p, \tag{25}$$

where $k_p = g/c_p^2$. Therefore, the height of the wave boundary layer increases with increasing c_p. Since the dominant phase speed of swell is of the order 15–25 m s^{-1}, the wave boundary layer is of the order 2–6 m deep. This gives a simple explanation for the height of the wave-driven jet.

c. Characteristics of the wave-driven jet

We now probe more deeply the dynamical processes that give rise to the wave-driven wind jet in order to develop a condition for the wave-driven wind and the magnitude of the jet.

Figure 8 shows profiles of the wind speed, u, total stress in the x direction, τ_x, and the partition of the total stress between the wave-induced, τ_w, and turbulent, τ_{tx}, parts for two cases with negative wave-induced stress: Fig. 8a shows $u_g = 2$ m s^{-1} and a wave-driven jet is produced; Fig. 8b shows $u_g = 5$ m s^{-1} and a wave-driven jet is not produced. In both cases the wave-induced stress is calculated for a spectrum of waves with $c_p = 20$ m s^{-1} and $u_s = 20$ m s^{-1}. In the first case with the wave-driven jet, there is a wind speed maximum at $z \approx h_i$. The gradient of the wind speed is positive within the wave boundary layer, corresponding to positive (downward) τ_{tx}, and negative (upward) above, corresponding to negative τ_{tx}. In the wave boundary layer the wave-induced stress has a magnitude greater than the turbulent stress so that the total stress is negative and approximately constant with height. Above the wave boundary layer the wave-induced stress rapidly falls off to zero so that the magnitude of the total stress decreases with height. In the second case, when no jet is produced, there is no wind speed maximum at the top of the wave boundary layer, so that the gradient of the wind speed is positive throughout the surface layer, corresponding to a positive turbulent stress, τ_{tx}. In this case the magnitude of the wave-induced stress is less than the turbulent stress; therefore the total stress is positive and decreases linearly with height with no constant stress layer in the wave boundary layer.

The essential dynamics of the wave-driven wind are therefore as follows: Within the wave boundary layer the wave-induced stress accelerates the wind because its vertical gradient is positive. The wind speeds within the wave boundary layer thus accelerate until balance is achieved with the frictional effects of the turbulent stress gradient, which decelerate the wind. The turbulent stress is particularly strong in the lower region of the wave boundary layer, near the surface, to bring the wind speed to zero to satisfy the no-slip boundary condition. This makes sense physically: the wave-induced stress provides the momentum to feed the jet, whereas the turbulent stress removes momentum from the jet; so for the jet to exist the feed must be greater than the loss. This is illustrated schematically in Fig. 9: the wave-induced stress transports momentum upward and the turbulent stress transports momentum away from the jet. Mathematically this corresponds to the necessary condition that $\tau_w(0)/u_*^2 < -1$, as discussed in section 4b.

An estimate for the speed of the jet can be obtained by analogy with the expression (12) for the jet speed obtained using the constant viscosity model. With the mixing length model, $K_m \approx u_* h_i$ at the top of the wave boundary layer. The simulations show that the wind profile below h_i has an approximately logarithmic variation with height. Therefore, the wind speed at the top of the wave boundary layer, $u_w = u\,(h_i)$, can then be estimated to be

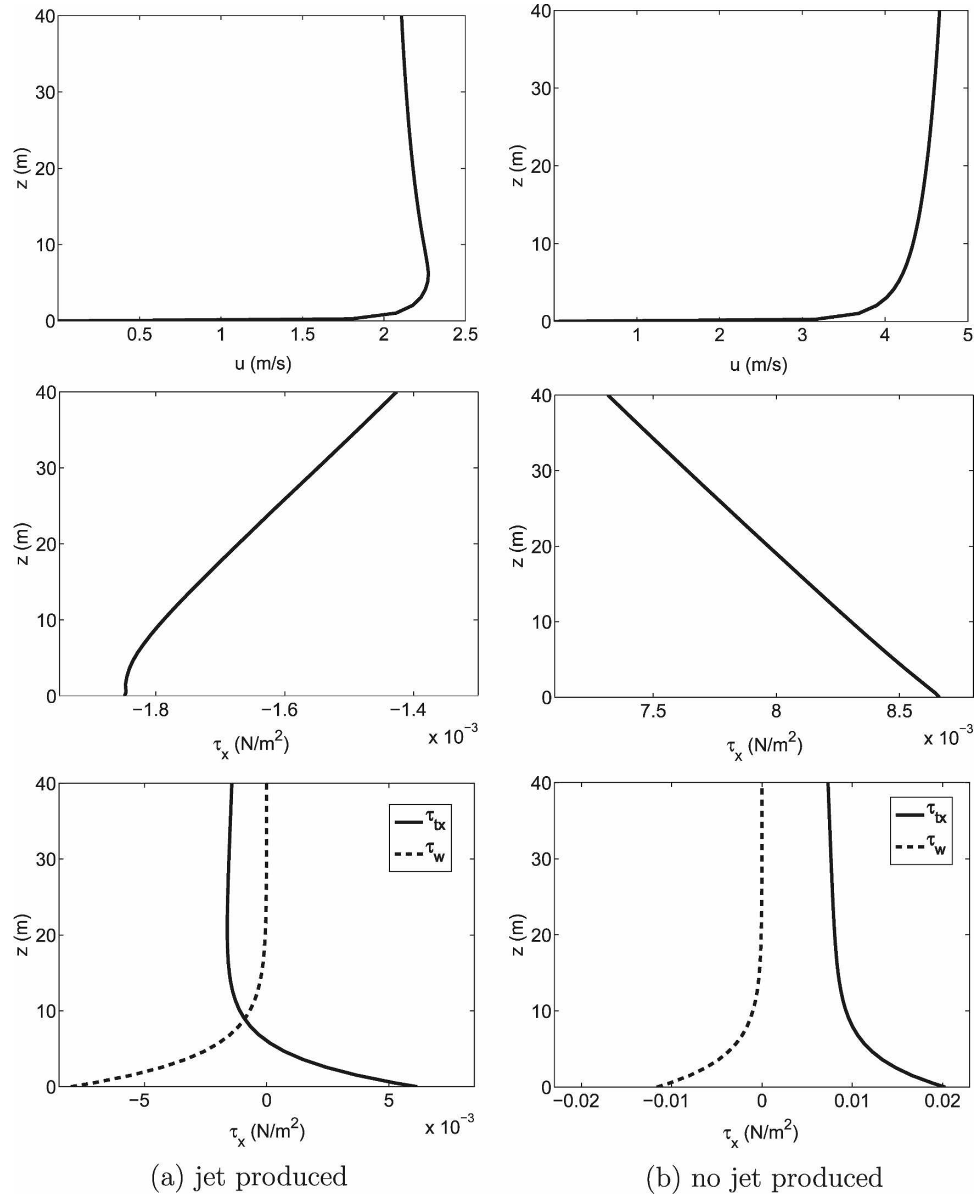

FIG. 8. Profiles of (top to bottom) the wind speed, u, total stress in the x direction, τ_x, and the partition of the total stress between wave induced, τ_ω, and turbulent, τ_{tx}: (a) $u_g = 2$ m s^{-1} and a wave-driven jet is produced and (b) $u_g = 5$ m s^{-1} and a wave-driven jet is not produced. In both cases $c_p = 20$ m s^{-1} and $u_s = 20$ m s^{-1}.

$$u_w \approx \frac{|\tau_w(0)|}{u_* \kappa} \ln(h_i/z_0). \tag{26}$$

The acceleration by the wave-induced stress then produces a supergeostrophic wave-driven jet if $u_w > u_g$.

To test this, u_w has been evaluated from numerical simulations with different values of u_g and u_s. The peak wave speed is kept constant: $c_p = 15$ m s^{-1}. Figure 10 shows u_w plotted against u_g. The filled symbols indicate when a jet was present in the u-wind profile. As predicted the line that separates jet from no jet is $u_w = u_g$.

The jet condition, $u_w > u_g$, can be written

$$\frac{|\tau_w(0)|}{u_*^2} \frac{u_*}{\kappa} \ln(h_i/z_0) > u_g, \tag{27}$$

which is a combination of two conditions. The first necessary condition is that the upward wave-induced momentum flux exceeds the downward turbulent momentum flux, $|\tau_w(0)|/u_*^2 > 1$. The second condition is that the wind speed at $z = h_i$ is larger than the geostrophic wind speed, so that a supergeostrophic jet is produced.

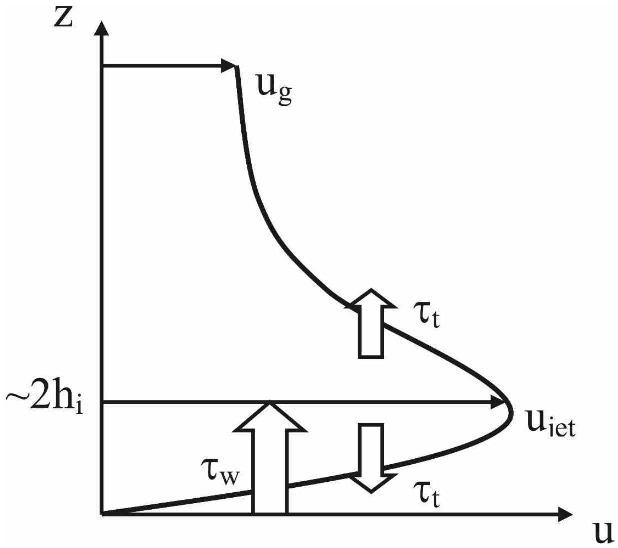

FIG. 9. Illustration to show the direction and relative magnitude of the momentum fluxes that produce a wave-driven jet. The wave-induced stress τ_ω acts to transport momentum upward in the wave boundary layer, whereas the turbulent stress τ_t acts to transport momentum away from the jet.

In Fig. 11 the jet strength, $u_{\max}$, is plotted against u_w for different values of u_s with $c_p = 15 \text{ m s}^{-1}$. Since u_w is the estimated speed of the jet we expect that $u_{\max} = u_w$. Figure 11 shows that the estimated speed of the jet, u_w, is usually greater than the actual speed of the jet, $u_{\max}$. A possible explanation for this is as follows: The height of the jet is actually closer to $2h_i$ than h_i. As the jet occurs above the wave boundary layer in the Ekman

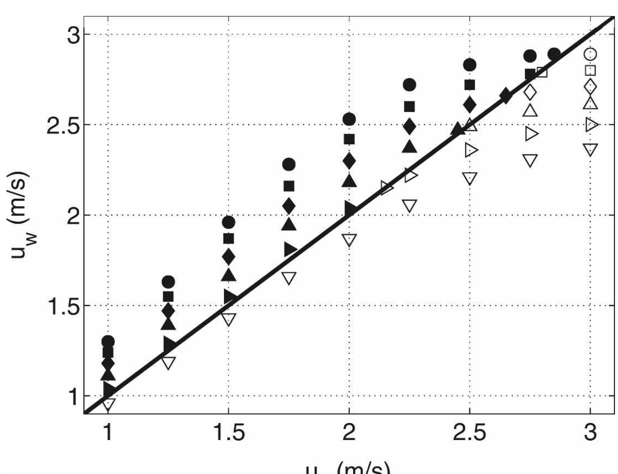

FIG. 10. Testing the condition for a wave-driven jet, $u_w > u_g$. Filled symbols indicate that a jet was present in the u-wind profile. Circles show the results for $u_s = 20 \text{ m s}^{-1}$, squares = 19, diamonds = 18, triangles pointing up = 17, and triangles pointing right = 16; and triangles pointing down show $u_c = 15$. In all runs $c_p = 15 \text{ m s}^{-1}$.

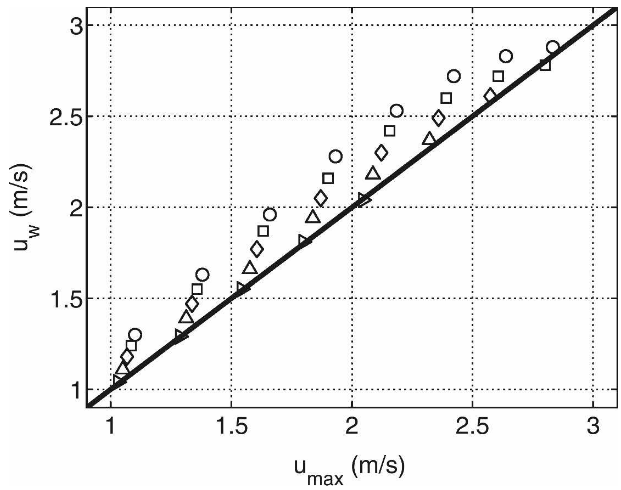

FIG. 11. The maximum jet speed, $u_{\max}$, against u_w. Circles show the results for $u_s = 20 \text{ m s}^{-1}$, squares = 19, diamonds = 18, triangles pointing up = 17, triangles pointing right = 16, and triangles pointing down = 15. In all runs $c_p = 15 \text{ m s}^{-1}$.

layer, the Ekman dynamics are acting to decrease the wind speed so that the maximum jet speed is not as large as it would be if the jet occurred at the top of the wave boundary layer.

5. Comparison with observations

Grachev and Fairall (2001) report the results of the San Clemente Ocean Probing Experiment (SCOPE) where the eddy correlation method was used to measure the turbulent momentum fluxes. During SCOPE, direct measurements of the sea surface wave parameters were also made. Their Fig. 4 shows individual 50-min averaged observations of the *uw* component of the momentum flux, τ_x, versus mean wind speed and inverse wave age, $U\cos\theta/c_p$. Their results show that the momentum flux changes sign in the range of $U\cos\theta/c_p$ from 0.05 to 0.2 where the wind speed is between 1 and 3 m s^{-1}.

The total stress, $\tau_w + \tau_t$, is negative at the surface if $\alpha = \tau_w(0)/u_*^2 < -1$. As argued in section 4b, the sign of α is mainly determined by c_p/u_*. Observations do not have access to τ_t and hence to u_*, as only the total stress, $\tau_w + \tau_t$, is easily measurable. Hence we tentatively use a value of the wind speed instead, so that the parameter becomes $c_p/U\cos\theta$. The component of the total stress in the x direction, $\tau_x(0)$, has been evaluated for a spectrum of waves of varying wave age. Figures 12a,b, respectively, show $\tau_x(0)$ versus inverse wave age, $(u_g\cos\theta)/c_p$, and the local wind speed, u_g. In agreement with the observations of Grachev and Fairall (2001), $\tau_x(0)$ reverses sign at an inverse wave age in the range of 0.15–0.2 where the wind speed is between 3 and 4 m s^{-1}. It is noted that the magnitude of the upward

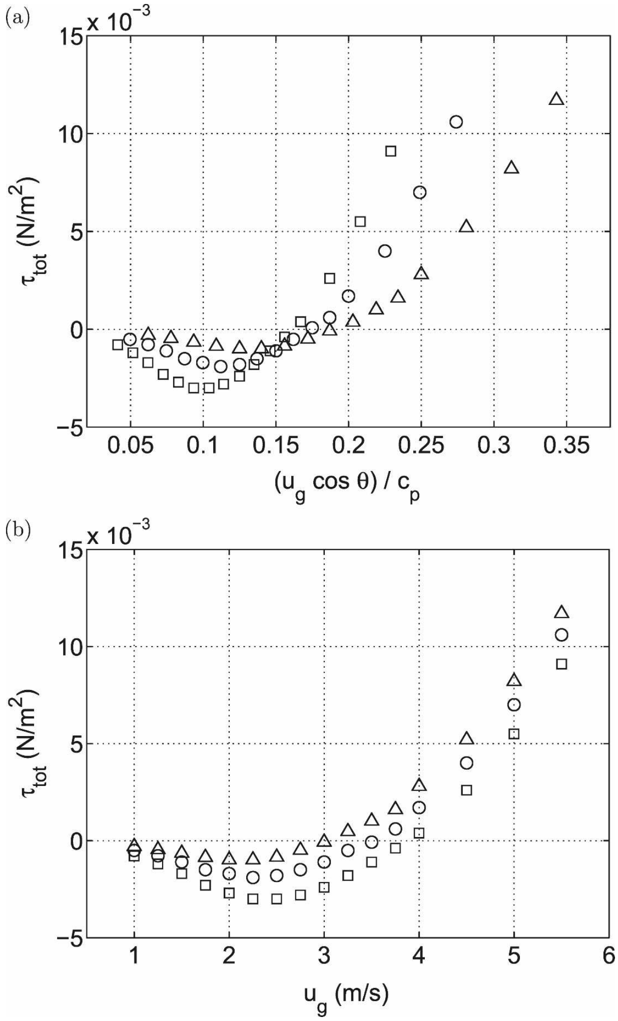

FIG. 12. The total stress, $\tau_{tot}(0)$, against (a) inverse wave age, $(u_g \cos\theta)/c_p$, and (b) wind speed, u_g. Squares, circles, and triangles show the results for model runs with $c_p = 24$, 20, and 16 m s^{-1}, respectively. In all runs $u_s = 20$ m s^{-1}.

momentum flux increases with increasing peak phase speed, c_p. This is because waves with a higher peak phase speed have more energy to impart to the wind. As a result, the maximum speed of the jet increases with c_p because there is more momentum to feed the jet.

The figures show that inverse wave age, $U\cos\theta/c_p$, is a good predictor of the change in sign of the total stress, and hence a first indicator of a wave-driven jet. The reason for this is that the transition from waves that take momentum from the wind to waves that give up momentum to the wind is determined by c_p/u_*, as described in section 4b. So the change in sign of τ_w is mainly determined by the value of $U\cos\theta/c_p$. But the inverse wave age is not sufficient to determine the magnitude of the wave-induced stress: for that the wave spectrum is required, as described in section 4b.

6. Conclusions

In this paper we have examined the role of ocean surface waves in shaping the wind profile in the marine atmospheric boundary layer. The focus has been the wave-driven wind regime, which observations suggest occurs when fast-moving swell propagates into regions of low geostrophic winds.

The wave-induced stress decays over a shallow depth of the order 5 m, and so it might be thought that the waves have little influence in controlling the dynamics of the boundary layer. Using the classical Ekman model augmented with a term representing the wave-induced stress, we have shown that when the upward momentum transfer from the waves exceeds the downward momentum flux by turbulence, the low-level wind is accelerated. When this acceleration is sufficiently large, a supergeostrophic wave-driven jet is produced at the top of the wave boundary layer. This thinking provides a condition for the occurrence of a supergeostrophic wave-driven jet, given in Eq. (26). The Coriolis force is therefore increased and balance is achieved with the boundary layer winds turning toward the synoptic high pressure (i.e., the winds turn in the opposite direction to the classical Ekman boundary layer). Hence we see that the whole marine boundary layer structure is changed in these circumstances, as also shown so persuasively by the LES experiments of Sullivan et al. (2008).

Next, the wave-induced stress was evaluated for a wave spectrum representing fast-moving swell. We argued that both dispersion and local dissipation processes tend to damp the short-wavelength, high-frequency components of the wind wave spectrum as it propagates away from the region of wave generation. The upward wave-induced stress then becomes greater than the downward turbulent stress when fast-moving, long-wavelength swell propagates into regions of low geostrophic wind. The main uncertainty in the quantitative calculation is the growth rate coefficient. Laboratory experiments could shed valuable light on its value in this regime.

These calculations also show that the wave-induced stress associated with swell is dominated by contributions from the peak in the swell spectrum, in contrast to wind-driven waves when the wave-induced stress is dominated by the very short-wavelength waves. Consequently, the depth of the wave boundary layer and hence also the height of the wave-driven jet can be estimated to be $0.1/k_p$, where k_p is the wavenumber of the waves at the peak in the spectrum. Additionally, the sign of the wave-induced stress, and hence the total momentum flux at the surface, are determined by the inverse wave age, $U\cos\theta/c_p$, because this parameter largely distinguishes the part of the swell spectrum that gives up momentum to the wind from the part of the swell spectrum that takes momentum from the wind. Calculations with the model show that the total stress changes sign from downward to upward when the inverse wave age drops below about 0.15–0.2, in rough agreement with ocean observations. We conclude that this condition provides a first practical estimate of the occurrence of wave-driven winds. The strength of the jet, however, requires a more precise estimate of the wave-induced stress, which in turn requires more detailed information about the wave spectrum.

These calculations help to clarify the dynamics of wave-driven winds and have determined a simple criterion to diagnose the occurrence of wave-driven winds, which in turn will help to determine the prevalence of this phenomenon across the world's oceans.

Acknowledgments. This work was made possible by a Ph.D. studentship funded by the Natural Environmental Research Council (NERC Reference NER/S/A/2003/11349A). We are grateful to Peter Sullivan for helpful discussions during the course of this work. We would also like to thank the reviewers for their thoughtful comments and suggestions.

REFERENCES

Alves, J. H., M. L. Banner, and I. R. Young, 2003: Revisiting the Pierson–Moskowitz asymptotic limits for fully developed wind waves. *J. Phys. Oceanogr.,* **33,** 1301–1323.

Belcher, S. E., and J. C. R. Hunt, 1993: Turbulent shear flow over slowly moving waves. *J. Fluid Mech.,* **251,** 109–148.

——, and J. C. R. Hunt, 1998: Turbulent flow over hills and waves. *Annu. Rev. Fluid Mech.,* **30,** 507–538.

Cohen, J. E., and S. E. Belcher, 1999: Turbulent shear flow over fast-moving waves. *J. Fluid Mech.,* **386,** 345–371.

Donelan, M. A., 1990: Air–sea interaction. *The Sea,* B. LeMehaute and D. M. Hanes, Eds., Ocean Engineering Science, Vol. 9, John Wiley and Sons, 239–291.

——, J. Hamilton, and W. H. Hui, 1985: Directional spectra of wind generated waves. *Philos. Trans. Roy. Soc. London,* **315,** 509–562.

——, W. M. Drennan, and K. B. Katsaros, 1997: The air–sea momentum flux in conditions of wind sea and swell. *J. Phys. Oceanogr.,* **27,** 2087–2099.

Drennan, W. M., H. C. Graber, D. Hauser, and C. Quentin, 2003: On the wave age dependence of wind stress over pure wind seas. *J. Geophys. Res.,* **108,** 8062, doi:10.1029/2000JC000715.

——, K. K. Kahma, and M. A. Donelan, 1999: On momentum flux and velocity spectra over waves. *Bound.-Layer Meteor.,* **92,** 489–515.

Edson, J., and Coauthors, 2007: The coupled boundary layers and air–sea transfer experiment in low winds. *Bull. Amer. Meteor. Soc.,* **88,** 341–356.

Grachev, A. A., and C. W. Fairall, 2001: Upward momentum transfer in the marine boundary layer. *J. Phys. Oceanogr.,* **31,** 1698–1711.

——, ——, J. E. Hare, J. B. Edson, and S. D. Miller, 2003: Wind stress vector over ocean waves. *J. Phys. Oceanogr.,* **33,** 2408–2429.

Hara, T., and S. E. Belcher, 2002: Wind forcing in the equilibrium range of wind-wave spectra. *J. Fluid Mech.,* **470,** 223–245.

Harris, D. L., 1966: The wave-driven wind. *J. Atmos. Sci.,* **23,** 688–693.

Hasselmann, D., and J. Bosenberg, 1991: Field measurements of wave-induced pressure over wind–sea and swell. *J. Fluid Mech.,* **230,** 391–428.

Janssen, P. A. E. M., 1989: Wave-induced stress and the drag of air flow over sea waves. *J. Phys. Oceanogr.,* **19,** 745–754.

Kudryavtsev, V. N., and V. K. Makin, 2004: Impact of swell on the marine atmospheric boundary layer. *J. Phys. Oceanogr.,* **34,** 934–949.

Kukulka, T., and T. Hara, 2005: Momentum flux budget analysis of wind-driven air-water interfaces. *J. Geophys. Res.,* **110,** C12020, doi:10.1029/2004JC002844.

Makin, V. K., V. N. Kudryavtsev, and C. Mastenbroek, 1995: Drag of the sea surface. *Bound.-Layer Meteor.,* **73,** 159–182.

Mastenbroek, C., 1996: Wind-wave interaction. Ph.D. thesis, Delft Technical University, 118 pp.

Meirink, J. F., and V. K. Makin, 2000: Modelling low-Reynolds-number effects in the turbulent air flow over water waves. *J. Fluid Mech.,* **415,** 155–174.

Phillips, O. M., 1966: *The Dynamics of the Upper Ocean*. 1st ed. Cambridge University Press, 336 pp.

——, 1985: Spectral and statistical properties of the equilibrium range in wind-generated gravity waves. *J. Fluid Mech.,* **156,** 505–531.

Pierson, W. J., and L. Moskowitz, 1964: A proposed spectral form for fully developed wind seas based on the similarity theory of S. A. Kitaigorodskii. *J. Geophys. Res.,* **69,** 5181–5190.

Plant, W. J., 1982: A relationship between wind stress and wave slope. *J. Geophys. Res.,* **87,** 1961–1967.

Polton, J. A., D. M. Lewis, and S. E. Belcher, 2005: The role of wave-induced Coriolis–stokes forcing on the wind-driven mixed layer. *J. Phys. Oceanogr.,* **35,** 444–457.

Smedman, A. S., M. Tjernström, and U. Högström, 1994: The near-neutral atmospheric boundary layer with no surface shearing stress: A case study. *J. Atmos. Sci.,* **51,** 3399–3411.

——, U. Högström, H. Bergström, A. Rutgersson, K. K. Kahma, and H. Pettersson, 1999: A case study of air–sea interaction during swell conditions. *J. Geophys. Res.,* **104,** 25 833–25 851.

——, X. G. Larsén, U. Högström, K. K. Kahma, and H. Pettersson, 2003: Effect of sea state on the momentum exchange over the sea during neutral conditions. *J. Geophys. Res.,* **108,** 3367, doi:10.1029/2002JC001526.

Snodgrass, F. E., G. W. Groves, K. F. Hasselman, G. R. Miller, W. H. Munk, and W. H. Powers, 1966: Propagation of ocean swell across the Pacific. *Philos. Trans. Roy. Soc. London,* **259,** 431–497.

Sullivan, P. P., J. C. McWilliams, and C.-H. Moeng, 2000: Simulation of turbulent flow over idealized water waves. *J. Fluid Mech.,* **404,** 47–85.

——, J. B. Edson, T. Hristov, and J. C. McWilliams, 2008: Large eddy simulations and observations of atmospheric marine boundary layers above non-equilibrium surface waves. *J. Atmos. Sci.,* **65,** 1225–1245.

Teixeira, M. A. C., and S. E. Belcher, 2002: On the distortion of turbulence by a progressive surface wave. *J. Fluid Mech.,* **458,** 229–267.